Nano Research

Open Access

Research Article

Fabrication of high-responsivity FET photodetector with $Ti_3C_2Cl_2$ MXene irradiated with 100 keV N ions

Zirong Liu[1,§], Shengyuan Peng[1,§], Qingyu Zhang[2], Mian Li[2], Yukun Xiao[2], Yuan Gao[1], Fangfang Ge[2], Xinwei Wang[4], Qing Huang[2] ✉, and Jianming Xue[1,3] ✉

[1] *State Key Laboratory of Nuclear Physics and Technology, School of Physics, Peking University, Beijing 100871, China*
[2] *Zhejiang Key Laboratory of Data-Driven High-Safety Energy Materials and Applications, Ningbo Key Laboratory of Special Energy Materials and Chemistry, Ningbo Institute of Materials Technology and Engineering, Chinese Academy of Sciences, Ningbo 315201, China*
[3] *CAPT and HEDPS, College of Engineering, Peking University, Beijing 100871, China*
[4] *School of Advanced Materials, Shenzhen Graduate School, Peking University, Shenzhen 518055, China*
§ *Zirong Liu and Shengyuan Peng contributed equally to this work.*

Cite this article: *Nano Research*, **2026**, *19*, 94908342. https://doi.org/10.26599/NR.2026.94908342

ABSTRACT: MXene has attracted intense attention in optoelectronic photodetectors due to its outstanding electrical conductivity and tunable electronic properties. By using the $Ti_3C_2Cl_2$ MXene irradiated with 100 keV N ions, a high-performance field-effect transistor (FET) photodetector was achieved and exhibited broadband photoresponse across the ultraviolet–visible–near infrared ray (UV–Vis–NIR) range. The responsivities of these FET photodetectors were as high as 5.3×10^4, 8.5×10^5, 3.3×10^4, and 2.8×10^5 A/W under 360, 550, 750, and 1060 nm light illumination, respectively, which are approximately two orders of magnitude higher than the other MXene-based photodetectors. The remarkable performance of the $Ti_3C_2Cl_2$ FET photodetector is attributed to synergistic effect of band gap and photoconductive gain. Besides, the ion fluence has significant influence on the photoresponse of the $Ti_3C_2Cl_2$ FET photodetector, and there exists an optimized ion fluence to obtain the highest responsivity. These findings highlight a controllable strategy for introducing band gap in MXenes and pave the way for their application in next-generation optoelectronic devices.

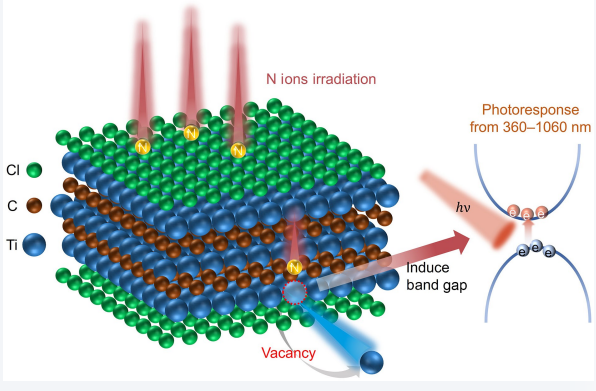

KEYWORDS: MXene, photodetector, ion irradiation, band gap

1 Introduction

MXenes are a class of emerging two-dimensional (2D) transition metal carbides and nitrides, generally represented by the formula $M_{n+1}X_nT_x$, where M denotes an early transition metal, X is carbon or nitrogen, and T_x refers to surface terminations such as –O, –OH, –F, or –Cl groups [1–4]. Owing to their exceptional physical properties, including ultrahigh electrical conductivity (8000–25,000 S/cm), tunable surface chemistry, mechanical flexibility, and over 90% optical transparency across the visible and infrared spectrum, MXenes have attracted increasing attention for applications in energy storage, electromagnetic shielding, and particularly in optoelectronics [5, 6].

Photodetectors, the key components in environmental monitoring, imaging sensing, and military detection technologies [7–10], have greatly benefited from 2D materials with tunable electronic and optical characteristics. Owing to excellent conductivity and optical transparency, previous studies primarily utilized MXenes as transparent electrodes or carrier transport layers. More recently, efforts have been made to explore their intrinsic photoresponse properties, particularly by constructing heterostructure devices to enhance their optoelectronic performance. For instance, integration with semiconductors such as MoS_2 [5], ZnO [6], Si [11], and perovskites [2, 12] has enabled broadband detection, self-powered operation, and flexible device configurations. These studies highlight the potential of MXene-based van der Waals heterostructures in achieving high-

Received: October 27, 2025; **Revised:** December 9, 2025
Accepted: December 14, 2025

✉Address correspondence to Qing Huang, huangqing@nimte.ac.cn; Jianming Xue, jmxue@pku.edu.cn

performance photodetection. However, most of these devices rely on the photoactivity of the semiconducting counterpart, while the intrinsic absorption of MXenes remains limited, which restricts their application as independent photoactive layers [13].

Recently, several works have suggested that MXenes themselves can participate in photodetection [14–16]. For instance, Alshareef and co-workers reported photodetectors fabricated by the broad plasmonic absorption of MXenes, in which Mo_2CT_x exhibited a responsivity as high as 9 A/W from the visible to near-infrared region, while Nb_2CT_x-$MAPbI_3$ showed a responsivity of 0.25 A/W under white light illumination [2]. Other studies revealed narrow-band photodetection behavior in Nb_2C within photoelectrochemical devices [17], as well as near-infrared photoconductivity in surface-functionalized $Ti_3C_2T_x$ [14]. Though significant progress has been achieved in fabricating high-performance photodetectors with MXene, there are still many challenges that have so far prevented MXenes from being systematically applied as photoactive media.

One of the challenges is to open the band gap of the MXenes since most of the as fabricated MXenes usually show metallic behavior and cannot be used as semiconducting devices directly. A range of strategies has been explored for band gap opening in 2D materials, including defect engineering [18], surface functionalization [19], and strain engineering [20]. Among these, defect engineering stands out as a particularly effective and scalable approach for opening a band gap, owing to its capacity to introduce well-defined electronic states via atomic-scale defects [21–24]. In general, ion irradiation offers a promising approach for the introduction of well-defined and controlled defects in 2D materials [25–27]. However, the irradiation effect on the band gap of MXene materials has so far not been investigated.

In this paper, we report the successful fabrication of field-effect transistor (FET) photodetector based on high-quality $Ti_3C_2Cl_2$ MXene irradiated with 100 keV N ions, and the device exhibits excellent broadband photoresponse covering the ultraviolet (UV) to near-infrared (360–1060 nm) range, with photoresponsivity 2 orders of magnitude higher than that of most existing 2D material-based phototransistors. Density functional theory (DFT) calculation was used to reveal the band gap of MXenes with irradiation induced defects. Besides, the ion fluence effect on the $Ti_3C_2Cl_2$ FET photodetector performance was also investigated experimentally.

2 Experimental

2.1 Materials synthesis of $Ti_3C_2Cl_2$ MXene

The $Ti_3C_2Cl_2$ MXene was synthesized by the "molten salt" method, as detailed in our previous reports [28–31]. A brief description was provided here: The raw materials of Ti_3AlC_2, $CdCl_2$, NaCl, and KCl were mixed and grinded together in a molar ratio of 1:5:20:20. The resulting powder mixture was placed into an aluminum oxide boat and heated to 700 °C with a heating rate of 5 °C/min under Ar atmosphere. After removing the byproduct with an aqueous HCl solution (1 mol/L) and washing with deionized water, the resulting solid was collected and dried under vacuum at 50 °C for 5 h, finally $Ti_3C_2Cl_2$ MXene was obtained.

2.2 Fabrication of $Ti_3C_2Cl_2$ FET

The synthesized $Ti_3C_2Cl_2$ was transferred onto a photolithographically pre-patterned SiO_2/Si substrate using a polydimethylsiloxane (PDMS) and dry transfer approach. The $Ti_3C_2Cl_2$ was positioned onto the designated location with the assistance of an optical microscope. The $Ti_3C_2Cl_2$ FET was fabricated following previously reported procedures [32, 33]. The source and drain electrodes were defined via the electron-beam lithography (EBL), and the metals (Ti/Au) were deposited by electron-beam evaporation.

2.3 Ion irradiation

The $Ti_3C_2Cl_2$ FET photodetectors were irradiated with 100 keV N ions. To investigate the influence of defect density on the electronic properties of $Ti_3C_2Cl_2$, the ion fluence ranged from 1×10^{12} to 1×10^{13} ions/cm^2 at a fixed fluence rate of 3×10^{11} ions/cm^2.

2.4 Measurement of optoelectronic properties of $Ti_3C_2Cl_2$ FET photodetector

The electronic properties of the pristine and irradiated $Ti_3C_2Cl_2$ FET photodetector were measured using a Keithley 4200A-SCS semiconductor analyzer. Photoresponse was excited using lasers at 360, 550, 750, and 1060 nm, with corresponding energy densities of 42.7, 88.3, 202.5, and 102.6 μW/cm^2, respectively. To minimize the temperature and ambient gas effects on the device performance, both dark current and at least two light-induced currents (excited by a specific wavelength) were measured, which ensured that there was no significant variation between the dark and light currents throughout the testing process.

2.5 DFT calculations

The calculations in this paper were based on the DFT using the Vienna *ab initio* simulation package (VASP). The ion-electron interaction was described by the projector augmented wave (PAW) method, and the exchange-correlation functional was described by the Perdew–Burke–Ernzerhof (PBE) [34–36]. For the plane-wave expansion, the plane-wave cutoff energy was set to 500 eV, and the convergence threshold was set at 1×10^{-6} eV/atom. The Monkhorst–Pack scheme was used for K-point sampling in the Brillouin zone, with a $4 \times 4 \times 1$ grid for geometry optimization and the static total energy calculation. A vacuum space of 22 Å was inserted to avoid the interaction of two $Ti_3C_2Cl_2$ MXene sheets. A 3×3 supercell was used for the $Ti_3C_2Cl_2$ with different types of vacancies [37].

3 Results and discussion

3.1 $Ti_3C_2Cl_2$ synthesis and characterization

$Ti_3C_2Cl_2$ MXene was synthesized via a molten salt-assisted method, using Ti_3AlC_2 as the precursor. The selective etching process was carried out in a mixture of $CdCl_2$, NaCl, and KCl at elevated temperature under an Ar atmosphere. After the reaction, the byproducts were removed by acid washing and the final product was thoroughly rinsed and vacuum-dried to obtain high-purity $Ti_3C_2Cl_2$ flakes. To confirm the structural integrity of $Ti_3C_2Cl_2$, X-ray diffraction (XRD) and energy-dispersive X-ray spectroscopy (EDS) were conducted. As shown in Fig. 1(a), the XRD pattern of the obtained $Ti_3C_2Cl_2$ exhibits a pronounced leftward shift of the (002) peak compared to the precursor Ti_3AlC_2, indicating an increased interlayer spacing due to the selective etching of the Al layers and the subsequent termination with Cl atoms. The disappearance of characteristic Ti_3AlC_2 peaks further confirms the effective

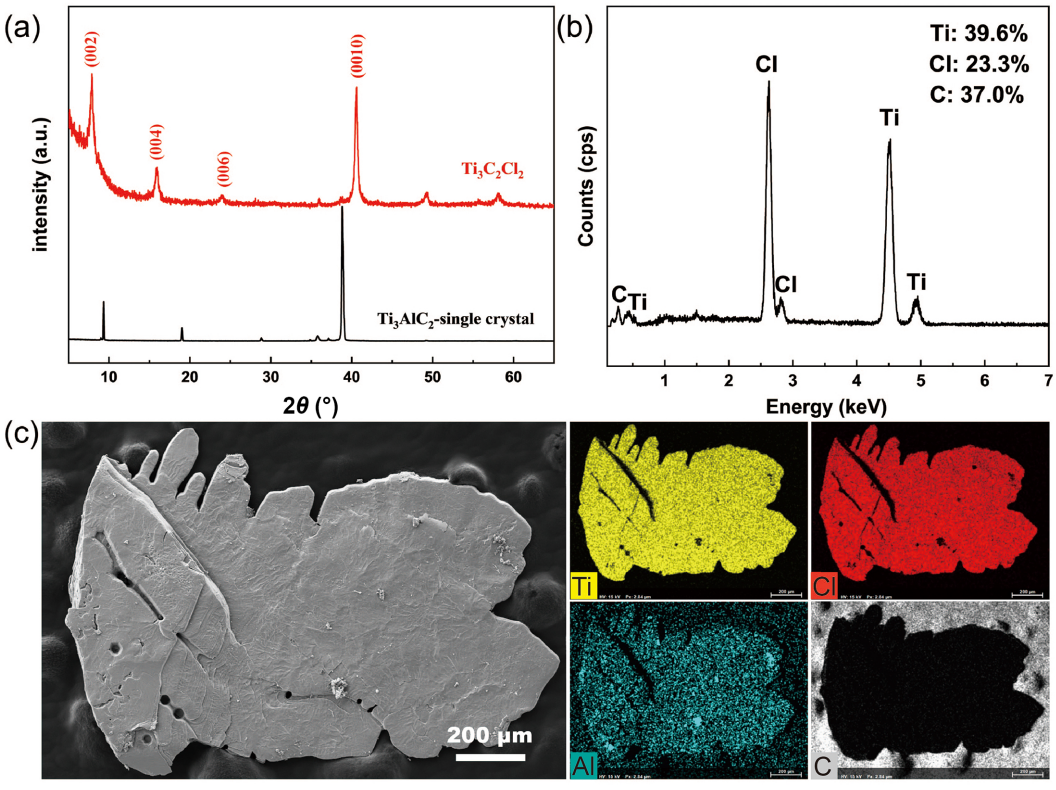

Figure 1 (a) XRD patterns of Ti_3AlC_2 precurso and the as-synthesized $Ti_3C_2Cl_2$ MXene. (b) Elemental composition of the as-synthesized $Ti_3C_2Cl_2$ MXene obtained with EDS. (c) SEM image of a $Ti_3C_2Cl_2$ flake along with EDS elemental mapping.

conversion from the MAX phase to the MXene phase. Additionally, the sharp and intense peaks of $Ti_3C_2Cl_2$ indicate its ordered crystal structure. The corresponding EDS analysis (Fig. 1(b)) reveals that the elemental composition of the MXene is Ti:C:Cl = 39.6:37.0:23.3 in atomic ratio, consistent with the stoichiometry of $Ti_3C_2Cl_2$, with negligible residual Al, demonstrating the complete etching of the A-site element. The clear presence of Cl also verifies the successful incorporation of Cl surface terminations during synthesis. Figure 1(c) shows the layered morphology of a $Ti_3C_2Cl_2$ flake. The corresponding EDS elemental mapping illustrates a homogeneous distribution of Ti, C, and Cl across the flake, suggesting uniform surface functionalization and high crystalline quality. Together, these results confirm the successful synthesis of phase-pure $Ti_3C_2Cl_2$ MXene with a well-defined layered structure and elemental composition, providing a reliable basis for subsequent property investigations.

3.2 Device characterization and ion irradiation design

$Ti_3C_2Cl_2$ FETs were fabricated on a substrate consisting of 285 nm SiO_2 on highly doped n-type silicon. To define the electrode patterns, a layer of electron beam resist was first spin-coated onto the substrate containing $Ti_3C_2Cl_2$, followed by electron-beam lithography. A 20 nm Ti/230 nm Au bilayer was deposited by electron-beam evaporation to form the contact electrodes. Finally, a lift-off process was performed to obtain the device structure shown in Fig. 2(a). Figure 2(b) is the image of the fabricated FET devices under optical microscopy; the red region represents the $Ti_3C_2Cl_2$ flake, and the white areas correspond to the metal electrodes. A more detailed description of the fabrication process can be found in the Experimental section.

The thickness of $Ti_3C_2Cl_2$ flake was measured to be about 110 nm using atomic force microscopy (AFM), as shown in Fig. 2(c). Figure 2(d) shows the depth distributions of the irradiation defect and N atom concentration at the ion fluence of 1×10^{12} ions/cm^2 were calculated with SRIM code with the quick Kinchin–Pease mode [38]. It can be clearly seen that most of the N ions penetrate the $Ti_3C_2Cl_2$ layer and rest within the SiO_2 layer, indicating that the effect of N atoms on the MXene layer could be neglected.

Figure S1 in the Electronic Supplementary Material (ESM) is the output curves of the pristine $Ti_3C_2Cl_2$ FET measured under dark conditions and under illumination at 360, 550, 750, and 1060 nm. All these curves exhibit nearly ideal Ohmic behavior within the bias range of −0.5 to 0.5 V, indicating that the as-prepared $Ti_3C_2Cl_2$ remained in a metallic state with no detectable light sensitivity.

3.3 Photodetection performance and mechanism of irradiated $Ti_3C_2Cl_2$ FETs

The current–voltage (I–V) characteristics of the irradiated $Ti_3C_2Cl_2$ FET photodetector at different ion fluences were measured under illumination at 360, 550, 750, and 1060 nm, respectively. To evaluate the performance of the $Ti_3C_2Cl_2$ FET photodetector, the photo responsivity (R) and detectivity (D) were calculated by

$$R_\lambda = I_{ph}/PA \quad (1)$$

$$D = R\sqrt{A/2eI_{dark}} \quad (2)$$

where I_{ph} ($= I_{light} - I_{dark}$) is photocurrent, P is the power density of the incident light, A is the effective area under illumination, and e is the charge of an electron.

The I–V curves of the $Ti_3C_2Cl_2$ FET photodetector exhibiting the

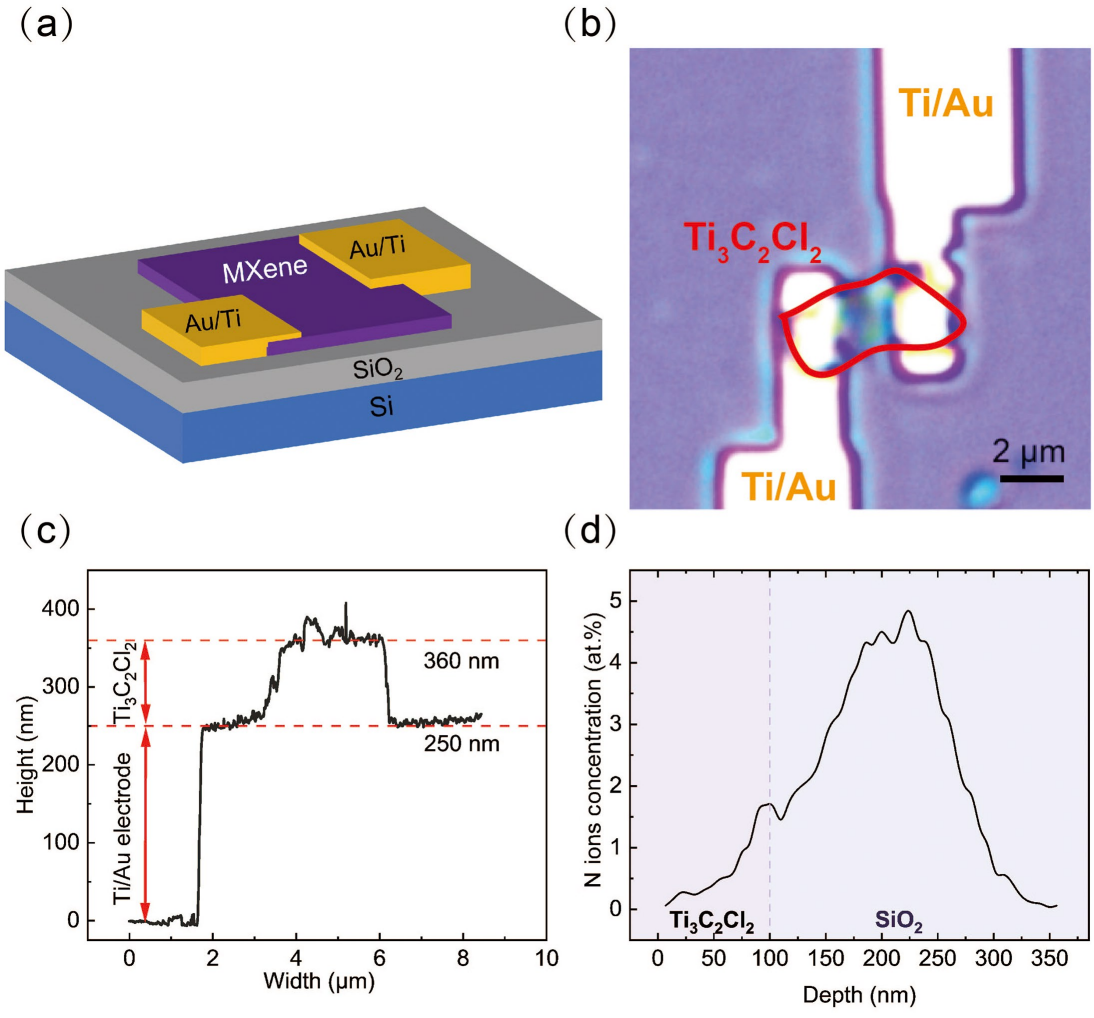

Figure 2 (a) The schematic of the $Ti_3C_2Cl_2$ FET photodetector. (b) Optical image of the $Ti_3C_2Cl_2$ FET photodetector. (c) AFM profiles of $Ti_3C_2Cl_2$ FET. (d) The depth distribution of implanted N ions calculated with SRIM code.

highest photoresponsivity at different wavelengths are shown in Fig. 3, and others irradiated at different ion fluences are shown in Figs. S2–S4 in the ESM. Figure 3 shows that, upon irradiation with N ions, the *I*–*V* characteristics of the irradiated $Ti_3C_2Cl_2$ FET photodetector exhibited a clear nonlinear behavior. This pronounced nonlinearity suggests the formation of a Schottky barrier at the metallic MXene interface, implying that the electronic structure of $Ti_3C_2Cl_2$ has been modified to exhibit semiconducting characteristics. Additionally, the irradiated samples displayed a significant photoresponse, further confirming the semiconducting transition. Therefore, ion irradiation can induce a metal-to-semiconductor transition in $Ti_3C_2Cl_2$, enabling the emergence of light-responsive behavior and Schottky-type electrical characteristics.

The corresponding *R* and *D* in the ultraviolet–visible–near infrared ray (UV–vis–NIR) region of these devices are also shown in Fig. 2. When the light wavelengths were 360, 550, 750, and 1060 nm, the responsivity reached as high as 5.4×10^4, 8.5×10^5, 3.3×10^4, and 2.8×10^5 A/W, while the corresponding detectivity was 1.3×10^{11}, 1.6×10^{12}, 1.0×10^{12}, and 7.8×10^{11} Jones (cm·Hz$^{1/2}$/W), respectively. All these measurements were conducted at a bias voltage of 0.5 V. Furthermore, the photoresponse times were less than 3 s as shown in Fig. S5 in the ESM.

The responsivity and detectivity of the irradiated $Ti_3C_2Cl_2$ FET photodetector are compared with those of previously reported MXene-based photodetectors [2, 5, 6, 11, 12, 39–44], as shown in Fig. 4. The highest photoresponsivity of the previously reported MXene-based photodetectors is in the order of 10^3 A/W [44]. Obviously, the photoresponsivities of the $Ti_3C_2Cl_2$ FET photodetector are more than two orders of magnitude higher. In addition, we compared the performance of our devices with those based on other well-studied 2D semiconductors, such as MoS_2, WSe_2, and InSe (Table 1). Remarkably, the irradiated $Ti_3C_2Cl_2$ FETs outperform these traditional 2D photodetectors in terms of both responsivity and detectivity. These results demonstrate not only the exceptional optoelectronic properties of defect-engineered $Ti_3C_2Cl_2$, but also its potential to expand the family of high-performance 2D material photodetectors toward practical applications in broadband photodetection.

To elucidate the underlying mechanism governing the evolution of the $Ti_3C_2Cl_2$ FET photodetector performance, first-principles calculation was performed. The unit cell of $Ti_3C_2Cl_2$ contains two inequivalent Ti positions (surface Ti and inner Ti, labeled as Ti1 and Ti2, respectively) and only one C position. Therefore, nine kinds of irradiation-induced defects were considered, and their structures are shown in Fig. S6 in the ESM. The formation energy

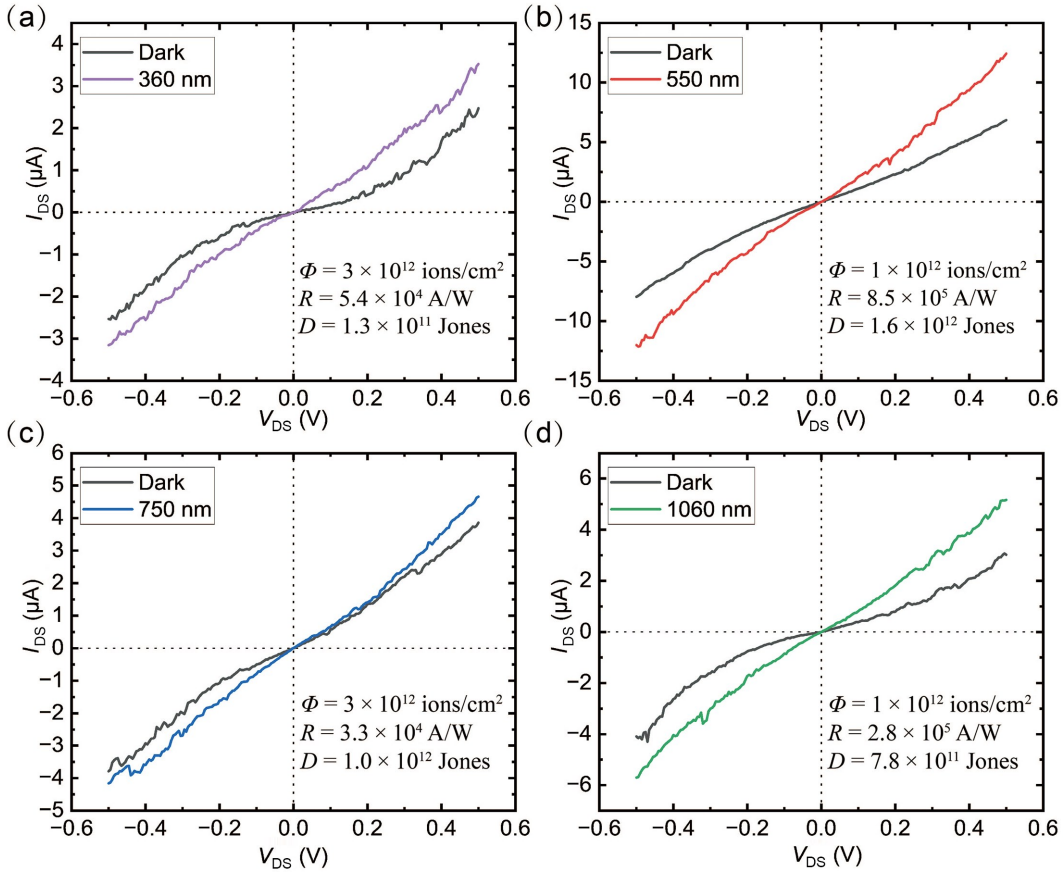

Figure 3 Current–voltage characteristics of the $Ti_3C_2Cl_2$ FET photodetector with the light wavelength of (a) 360 nm, (b) 550 nm, (c) 750 nm, and (d) 1060 nm.

of the defects and the impact of irradiation-induced defects on the band gap of the device were calculated, as shown in Table S1 in the ESM. The calculation results reveal that single vacancies, including V_{Ti}, V_{Ti2}, and V_C, cannot open a band gap in the $Ti_3C_2Cl_2$, and the $Ti_3C_2Cl_2$ FETs exhibit metallic properties, which is consistent with the previous reports [37, 50]. However, the introduction of $V_{Ti1+Ti1}$, $V_{Ti1+Ti2}$, and $V_{Ti1+Ti2+C}$ leads to the band gap opening, as shown in Fig. 5, consequently resulting in distinct alterations in the optoelectronic properties of the device. Based on experimental observations and first-principles calculations, we found that single vacancies in $Ti_3C_2Cl_2$ were insufficient to induce a band gap opening, and consequently, the $Ti_3C_2Cl_2$ FETs exhibited no photoresponse. As the ion fluence increased to 1×10^{12} and 3×10^{12} ions/cm^2—corresponding to estimated defect densities of 3.4×10^{20} and 1×10^{21} atoms/cm^3, respectively—single vacancies began to evolve into complex multi-vacancy configurations such as $V_{Ti1+Ti1}$, $V_{Ti1+Ti2}$, and $V_{Ti1+Ti2+C}$. First-principles calculations confirm that these multi-vacancy defects are capable of opening a finite band gap in $Ti_3C_2Cl_2$, resulting in a transition from metallic to semiconducting behavior and enabling a pronounced photoresponse in the irradiated FETs.

Based on the above results, the ultrahigh photoresponsivity observed in our $Ti_3C_2Cl_2$ FET photodetector can be attributed to the synergistic effect of band-gap-assisted electron-hole pair generation and photoconductive gain. The narrow band gap facilitates intrinsic light absorption, thereby enabling efficient photocarrier generation and collection by the electrodes. Moreover, ion irradiation introduces localized trap states that can capture photogenerated carriers and suppress their rapid recombination, thereby effectively prolonging the carrier lifetime. This trap-assisted lifetime extension is consistent with the 0.6 and 2.4 s response time observed in our experiments (shown in Fig. S5 in the ESM). Previous experimental and theoretical studies have reported carrier mobilities of single-layer $Ti_3C_2T_x$ in the range of 10^2–10^4 cm^2/(V·s) [51, 52]. Based on the photoconductive gain calculation method, the photoconductive gain (G) could be calculated by [53]

$$G = \tau_{life}/\tau_{transit} = \tau_{life}\mu V_{DS}/L^2 \quad (3)$$

where τ_{life} is the carrier lifetime, $\tau_{transit}$ is the transit time, μ is the carrier mobility, and L is the channel length, and the upper limit of R could be estimated by

$$R_{upper} = I_{ph}/P = G\eta q/h\nu \quad (4)$$

where η is the external quantum efficiency, q is the elementary charge, and $h\nu$ is the energy of a photon. Our $Ti_3C_2Cl_2$ FET photodetector achieves an ultrahigh photoconductive gain exceeding 10^8 even when the mobility is estimated at 10^2 cm^2/(V·s). This gain mechanism allows photogenerated carriers to recirculate within the channel multiple times, greatly amplifying the photocurrent signal and resulting in a theoretical upper limit R in the range of 10^6–10^7 A/W. The use of Ti/Au electrodes ensures low-barrier contacts, facilitating efficient carrier injection and collection. In summary, the combination of a narrow bandgap, high carrier mobility, and defect-engineered carrier dynamics collectively explains the ultrahigh responsivity achieved in our $Ti_3C_2Cl_2$ FET photodetector.

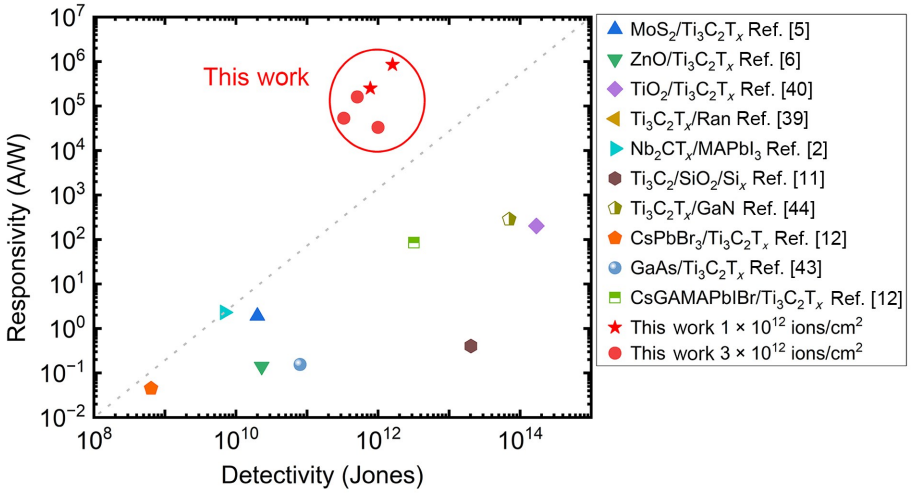

Figure 4 Comparison of responsivity and detectivity of the irradiated $Ti_3C_2Cl_2$ FET photodetector with other MXene-based photodetectors.

Table 1 Comparison of optoelectronic properties of 2D materials photodetectors

Materials	V_{DS} (V)	Wavelength (nm)	Responsivity (A/W)	Detectivity (Jones)	Ref.
Monolayer MoS_2	10	532	3.5	—	[45]
	3	632	15.6	—	[46]
Multilayer MoS_2	0.2	633	0.12	—	[47]
	1	980	2.3	—	[48]
WSe_2/graphene	0.5	532	2.05	—	[34]
	0.5	1064	1.06×10^{-3}	—	[34]
$MoTe_2$	0	1060	2.4×10^{-3}	1×10^{8}	[35]
$MoTe_2/ReS_2$	−3	808	0.9	1×10^{10}	[36]
Graphene/$MoTe_2$/graphene	0	1064	0.11	1×10^{8}	[49]
MXene (1×10^{12} ions/cm^2)	0.5	550	8.5×10^{5}	1.6×10^{12}	This work
	0.5	1060	2.8×10^{5}	7.8×10^{11}	This work
MXene (3×10^{12} ions/cm^2)	0.5	360	5.3×10^{4}	1.3×10^{11}	This work
	0.5	550	1.6×10^{5}	5.11×10^{11}	This work
	0.5	750	3.3×10^{4}	1×10^{12}	This work

3.4 Fluence-dependent photoresponsivity in irradiated $Ti_3C_2Cl_2$ FETs

It should be emphasized that the optimal photodetection performance of $Ti_3C_2Cl_2$ FETs for different light wavelengths was obtained at different ion fluences, namely defect densities in the irradiated MXene. Figure 4 shows the dependence of the responsivity of the $Ti_3C_2Cl_2$ FET photodetector on the defect density at different light wavelengths. The defect density introduced by N ion irradiation was calculated using the SRIM code and NRT model. In the NRT model, the vacancy yields (N_E) are estimated by the equation $N_E = 0.8\nu(E)/2T_d$, where $\nu(E)$ is the energy of nuclear loss and T_d is the displacement threshold of the lattice atom [54]. $\nu(E)$ for N ions in $Ti_3C_2Cl_2$ can be calculated using SRIM code, and T_d is estimated from DFT calculations. The calculated vacancy yields of the surface Ti (Ti_1), inner Ti (Ti_2), and C were 1.12, 1, 1.32 /(Å·ion), respectively. Based on these values, the target vacancy densities were set in the range of 3.4×10^{20} to 3.4×10^{21} atoms/cm^3, corresponding to defect concentrations from 0.9% to 9%.

As shown in Fig. 6, the photoresponse of $Ti_3C_2Cl_2$ FET photodetector increased significantly with the initial introduction of defect, reaching its peak at relatively low influences (1×10^{12} to 3×10^{12} ions/cm^2). This enhancement can be attributed to the defect-induced modulation of the electronic structure, which facilitates band gap opening and promotes efficient photocarrier generation and separation. Similar phenomena have been reported in previous studies [22–24], where moderate defect engineering was shown to improve the optoelectronic properties of 2D materials by tailoring their band structures. However, as the defect density continued to increase, the photoresponse began to deteriorate and eventually vanished. This suppression can be explained by the excessive accumulation of structural disorder, which is reported to severely degrade carrier mobility, reduce photocarrier lifetime, and, in extreme cases, disrupt the crystal structure entirely [55, 56]. In our case, the rapid drop in photoresponse at high irradiation fluences, accompanied by the reappearance of linear I–V characteristics, strongly suggests a transition back to metallic behavior likely caused by structural collapse or amorphization of the MXene lattice. There exists an optimal defect density for maximizing the photoresponse, and the ion fluence used in this study can be easily achieved, with the highest fluence requiring just one minute of irradiation. This highlights the efficiency and convenience of ion irradiation as a method for precisely controlling defect density, making it an effective and accessible approach for developing high-performance MXene-based photodetectors.

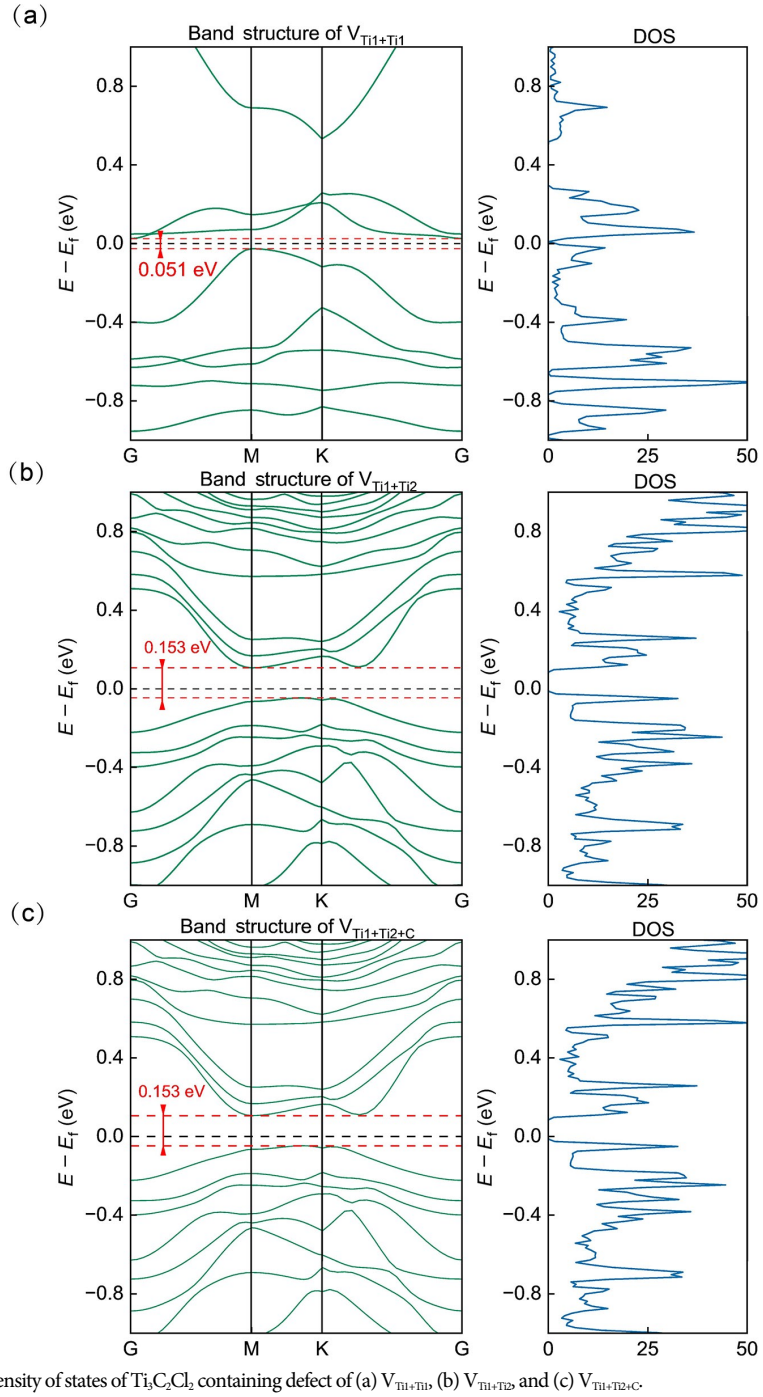

Figure 5 The band structure and density of states of $Ti_3C_2Cl_2$ containing defect of (a) $V_{Ti1+Ti1}$, (b) $V_{Ti1+Ti2}$, and (c) $V_{Ti1+Ti2+C}$.

To investigate the impact of ion irradiation on the lattice structure of $Ti_3C_2Cl_2$, Raman spectroscopy was performed on samples irradiated at different ion fluences. To minimize the influence of environmental factors such as air exposure and temperature fluctuations, five $Ti_3C_2Cl_2$ samples were prepared under identical conditions and irradiated with varying ion fluences before characterization, and the results at different ion fluences were normalized based on their pristine spectra. The normalized Raman spectra of $Ti_3C_2Cl_2$ shown in Fig. 7 exhibit two prominent Raman-active modes located at ~ 220 cm^{-1} (A_g) and ~ 620–660 cm^{-1} (E_g), consistent with previous reports [57, 58]. Upon ion irradiation, a progressive decrease in the intensity of both peaks was observed with increasing fluences. Notably, the peak positions of both A_g and E_g modes remained nearly unchanged, suggesting that the basic vibrational symmetry of the lattice is initially preserved despite the introduction of defects. However, the trend in intensity degradation offers further insight. At lower ion fluences (1×10^{12} to 7×10^{12} ions/cm^2), the Raman peaks gradually weakened, indicating the formation of point defects and partial lattice disorder without significant structural collapse. This regime correlates well with the earlier observation of enhanced photoresponse, which is likely promoted by these moderate defect concentrations. In contrast, at higher fluences (1×10^{13} ions/cm^2), both A_g and E_g peaks nearly vanished, indicating severe structural degradation or even amorphization of the $Ti_3C_2Cl_2$ lattice. This structural collapse aligns with the sharp decline in photoresponse and the re-emergence of

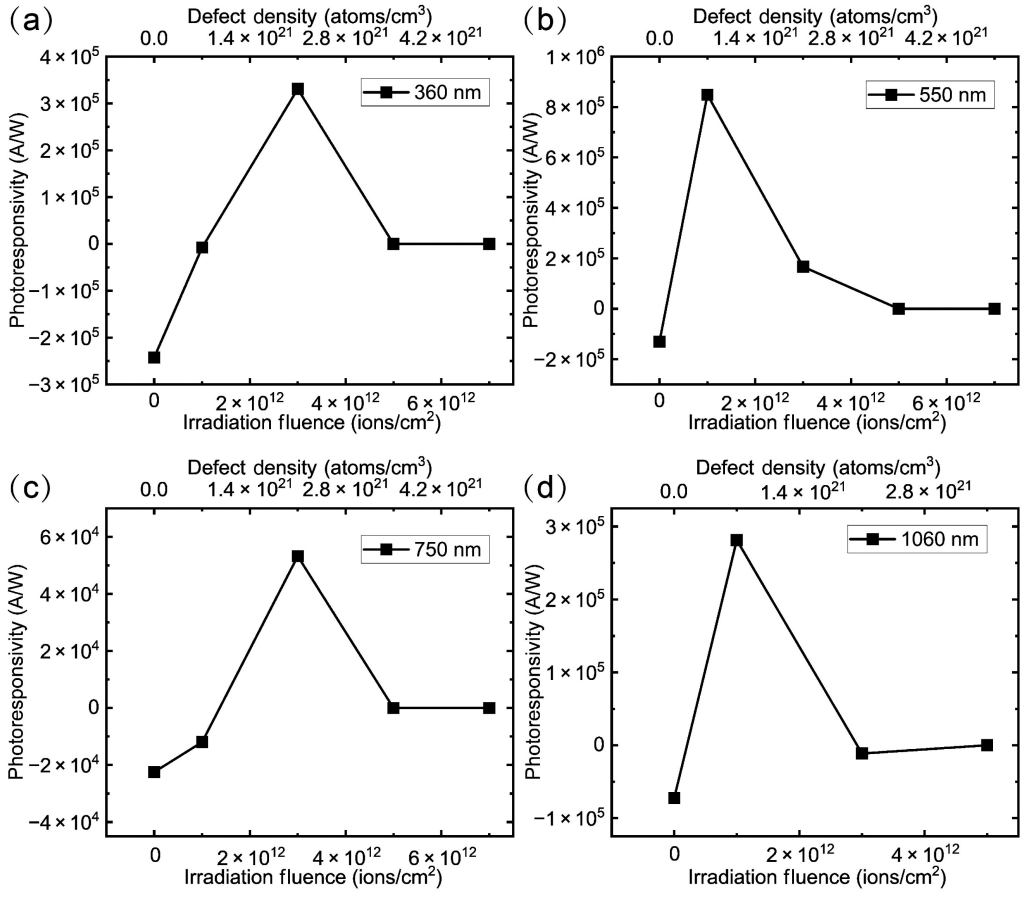

Figure 6 Dependence of the $Ti_3C_2Cl_2$ FET responsivity on ion fluence at light wavelength of (a) 360 nm, (b) 550 nm, (c) 750 nm, and (d) 1060 nm.

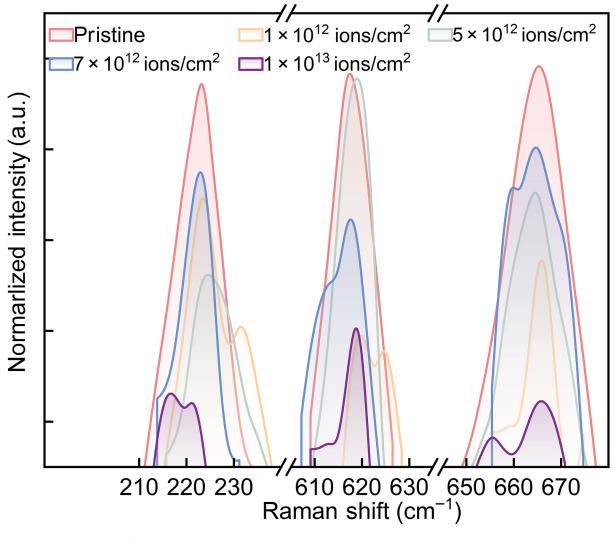

Figure 7 Normalized Raman spectra of pristine $Ti_3C_2Cl_2$ and samples irradiated at different ion fluence.

metallic conductivity, as discussed previously. The Raman results therefore support the conclusion that a critical ion fluence exists beyond which the defect-induced band structure modulation is no longer beneficial. These findings highlight the dual role of ion irradiation—serving as both a tool for band gap engineering and a potential source of structural destruction, emphasizing the importance of optimizing irradiation conditions to balance defect formation and structural integrity.

4 Conclusions

We have fabricated a high-performance photodetector with $Ti_3C_2Cl_2$ MXene through N ion irradiation which exhibit excellent detectivity at low operating voltages and a responsivity that exceeds other MXene based photodetectors by two orders of magnitude. This remarkable performance is ascribed to the irradiation-induced band gap opening and photoconductive gain, which synergistically enable efficient photocarrier generation and prolonged carrier lifetimes. Furthermore, the dependence of device responsivity on ion fluence reveals an optimal irradiation condition for different light wavelengths. These findings highlight a controllable strategy for introducing band gap in MXenes and pave the way for their application in next-generation optoelectronic devices. These findings highlight ion-beam irradiation as an efficient strategy for introducing a band gap in MXenes and broadening their application potential in high-performance broadband optoelectronic devices.

Electronic Supplementary Material: Supplementary material (optoelectronic properties of pristine and irradiated MXene, geometric structures for DFT and formation energies) is available in the online version of this article at https://doi.org/10.26599/NR.2026.94908342.

Data availability

All data needed to support the conclusions in the paper are presented in the manuscript and the Electronic Supplementary

Material. Additional data related to this paper may be requested from the corresponding author upon request.

Acknowledgements

This work was supported by the National Natural Science Foundation of China (Nos. 12435017, 12275336, and U23A2093). The authors are grateful for the computing resources provided by the High Performance Computing Platform of the Center for Life Science of Peking University, and the Weiming No. 1 and Life Science No.1 High Performance Computing Platform at Peking University.

Declaration of competing interest

All the contributing authors report no conflict of interests in this work.

Author contribution statement

Z. R. L.: Investigation, data curation, formal analysis, writing – original draft. S. Y. P.: Investigation, data curation, formal analysis, writing – original draft. Q. Y. Z.: Investigation, data curation, validation. M. L.: Resources, methodology. Y. K. X.: Resources, methodology. Y. G.: Resources, validation, methodology. F. F. G.: Resources, methodology. X. W. W.: Resources, methodology. Q. H.: Conceptualization, supervision, project administration, funding acquisition, writing – review & editing. J. M. X.: Conceptualization, supervision, project administration, funding acquisition, writing – review & editing. All the authors have approved the final manuscript.

Use of AI statement

None.

References

[1] Li, R. Y.; Zhang, L. B.; Shi, L.; Wang, P. MXene Ti_3C_2: An effective 2D light-to-heat conversion material. *ACS Nano* **2017**, *11*, 3752–3759.

[2] Liu, Z. X.; El-Demellawi, J. K.; Bakr, O. M.; Ooi, B. S.; Alshareef, H. N. Plasmonic Nb_2CT_x MXene-$MAPbI_3$ heterostructure for self-powered visible-NIR photodiodes. *ACS Nano* **2022**, *16*, 7904–7914.

[3] Chen, X.; Shi, Z. F.; Tian, Y. T.; Lin, P.; Wu, D.; Li, X. J.; Dong, B.; Xu, W.; Fang, X. S. Two-dimensional Ti_3C_2 MXene-based nanostructures for emerging optoelectronic applications. *Mater. Horiz.* **2021**, *8*, 2929–2963.

[4] Sreedhar, A.; Ta, Q. T. H.; Noh, J. S. Versatile role of 2D Ti_3C_2 MXenes for advancements in the photodetector performance: A review. *J. Ind. Eng. Chem.* **2023**, *127*, 1–17.

[5] Zhu, J. T.; Wang, H.; Ma, L.; Zou, G. F. Observation of ambipolar photoresponse from 2D MoS_2/MXene heterostructure. *Nano Res.* **2021**, *14*, 3416–3422.

[6] Zheng, T. X.; Wang, W. W.; Du, Q. Y.; Wan, X.; Jiang, Y. F.; Yu, P. P. 2D Ti_3C_2-MXene nanosheets/ZnO nanorods for UV photodetectors. *ACS Appl. Nano Mater.* **2024**, *7*, 3050–3058.

[7] Wu, D.; Guo, J. W.; Wang, C. Q.; Ren, X. Y.; Chen, Y. S.; Lin, P.; Zeng, L. H.; Shi, Z. F.; Li, X. J.; Shan, C. X. et al. Ultrabroadband and high-detectivity photodetector based on WS_2/Ge heterojunction through defect engineering and interface passivation. *ACS Nano* **2021**, *15*, 10119–10129.

[8] Wang, Q. S.; Lai, J. W.; Sun, D. Review of photo response in semiconductor transition metal dichalcogenides based photosensitive devices. *Opt. Mater. Express* **2016**, *6*, 2313–2327.

[9] Sredenschek, A. J.; Sanchez, D. E.; Wang, J. Y.; Lei, Y.; Sinnott, S. B.; Terrones, M. Heterostructures coupling ultrathin metal carbides and chalcogenides. *Nat. Mater.* **2024**, *23*, 460–469.

[10] Wang, X. X.; Wang, S. F.; Wu, Y. W.; Wang, W. H.; Cao, Z. Y.; Wei, B. B.; Han, T.; Li, F.; Wang, S. L.; Shan, L. et al. A self-powered photodetector based on graphene enhanced WSe_2/$PtSe_2$ heterodiode with fast speed and broadband response. *Adv. Opt. Mater.* **2024**, *12*, 2400052.

[11] Kang, Z.; Ma, Y. N.; Tan, X. Y.; Zhu, M.; Zheng, Z.; Liu, N. S.; Li, L. Y.; Zou, Z. G.; Jiang, X. L.; Zhai, T. Y. et al. MXene-silicon van Der Waals heterostructures for high-speed self-driven photodetectors. *Adv. Electron. Mater.* **2017**, *3*, 1700165.

[12] Deng, W.; Huang, H. C.; Jin, H. M.; Li, W.; Chu, X.; Xiong, D.; Yan, W.; Chun, F.; Xie, M. L.; Luo, C. et al. All-sprayed-processable, large-area, and flexible perovskite/MXene-based photodetector arrays for photocommunication. *Adv. Opt. Mater.* **2019**, *7*, 1801521.

[13] Xu, D. X.; Li, Z. D.; Li, L. S.; Wang, J. Insights into the photothermal conversion of 2D MXene nanomaterials: Synthesis, mechanism, and applications. *Adv. Funct. Mater.* **2020**, *30*, 2000712.

[14] Hu, C. Q.; Du, Z. J.; Wei, Z. M.; Li, L.; Shen, G. Z. Functionalized $Ti_3C_2T_x$ MXene with layer-dependent band gap for flexible NIR photodetectors. *Appl. Phys. Rev.* **2023**, *10*, 021402.

[15] Hu, C. Q.; Wei, Z. M.; Li, L.; Shen, G. Z. Strategy toward semiconducting $Ti_3C_2T_x$-MXene: Phenylsulfonic acid groups modified $Ti_3C_2T_x$ as photosensitive material for flexible visual sensory-neuromorphic system. *Adv. Funct. Mater.* **2023**, *33*, 2302188.

[16] Li, L.; Shen, G. Z. MXene based flexible photodetectors: Progress, challenges, and opportunities. *Mater. Horiz.* **2023**, *10*, 5457–5473.

[17] Gao, L. F.; Ma, C. Y.; Wei, S. R.; Kuklin, A. V.; Zhang, H.; Ågren, H. Applications of few-layer Nb_2C MXene: Narrow-band photodetectors and femtosecond mode-locked fiber lasers. *ACS Nano* **2021**, *15*, 954–965.

[18] Fan, X. F.; Shen, Z. X.; Liu, A. Q.; Kuo, J. L. Band gap opening of graphene by doping small boron nitride domains. *Nanoscale* **2012**, *4*, 2157–2165.

[19] Xu, J. Y.; Yu, J. S.; Liao, J. H.; Yang, X. B.; Wu, C. Y.; Wang, Y.; Wang, L.; Xie, C.; Luo, L. B. Opening the band gap of graphene via fluorination for high-performance dual-mode photodetector Application. *ACS Appl. Mater. Interfaces* **2019**, *11*, 21702–21710.

[20] He, K. L.; Poole, C.; Mak, K. F.; Shan, J. Experimental demonstration of continuous electronic structure tuning via strain in atomically thin MoS_2. *Nano Lett.* **2013**, *13*, 2931–2936.

[21] Zhu, H. P.; Tang, Y. J.; Zhong, A. X.; Wang, L.; Liu, F. Y.; Zhao, P. X.; Liu, J.; Shu, L.; Wu, Z. P.; Li, B. Swift heavy ion irradiation-driven energy band engineering and its profound influence on the photoresponse of β-Ga_2O_3 ultraviolet photodetectors. *Appl. Phys. Lett.* **2024**, *124*, 153505.

[22] Ma, L.; Tan, Y.; Ghorbani-Asl, M.; Boettger, R.; Kretschmer, S.; Zhou, S.; Huang, Z.; Krasheninnikov, A. V.; Chen, F. Tailoring the optical properties of atomically-thin WS_2 via ion irradiation. *Nanoscale* **2017**, *9*, 11027–11034.

[23] Chen, Y.; Huang, S. X.; Ji, X.; Adepalli, K.; Yin, K. D.; Ling, X.; Wang, X. W.; Xue, J. M.; Dresselhaus, M.; Kong, J. et al. Tuning electronic structure of single layer MoS_2 through defect and interface engineering. *ACS Nano* **2018**, *12*, 2569–2579.

[24] Chen, R. C.; Liu, G. L.; Qiu, F.; Tan, Y.; Chen, F. Self-powered waveguide-integrated photodetector based on a defect-engineered WSe_2/graphene heterojunction. *Opt. Mater. Express* **2022**, *12*, 3614–3620.

[25] Lin, Z.; Carvalho, B. R.; Kahn, E.; Lv, R. T.; Rao, R.; Terrones, H.; Pimenta, M. A.; Terrones, M. Defect engineering of two-dimensional transition metal dichalcogenides. *2D Mater.* **2016**, *3*, 022002.

[26] Gupta, D.; Chauhan, V.; Upadhyay, S.; Koratkar, N.; Singh, F.; Kumar, S.; Mahajan, A.; Chandra, R.; Kumar, R. Defects engineering and enhancement in optical and structural properties of 2D-MoS_2 thin films by high energy ion beam irradiation. *Mater. Chem. Phys.* **2022**, *276*, 125422.

[27] Jiang, J.; Ling, C. Y.; Xu, T.; Wang, W. H.; Niu, X. H.; Zafar, A.; Yan, Z. Z.; Wang, X. M.; You, Y. M.; Sun, L. T. et al. Defect engineering for modulating the trap states in 2D photoconductors. *Adv. Mater.* **2018**, *30*, 1804332.
[28] Li, M.; Lu, J.; Luo, K.; Li, Y. B.; Chang, K. K.; Chen, K.; Zhou, J.; Rosen, J.; Hultman, L.; Eklund, P. et al. Element replacement approach by reaction with Lewis acidic molten salts to synthesize nanolaminated MAX phases and MXenes. *J. Am. Chem. Soc.* **2019**, *141*, 4730–4737.
[29] Liu, X. B.; Li, Y. B.; Ding, H. M.; Chen, L.; Du, S. Y.; Chai, Z. F.; Huang, Q. Topotactic transition of Ti_4AlN_3 MAX phase in lewis acid molten salt. *J. Materiomics* **2023**, *9*, 1032–1038.
[30] Zhou, J.; Zha, X.; Zhou, X. B.; Chen, F. Y.; Gao, G. L.; Wang, S. W.; Shen, C.; Chen, T.; Zhi, C. Y.; Eklund, P. et al. Synthesis and electrochemical properties of two-dimensional hafnium carbide. *ACS Nano* **2017**, *11*, 3841–3850.
[31] Deng, T. Y.; Sun, J. R.; Tai, P. F.; Wang, Y. Y.; Zhang, L. Q.; Chang, H. L.; Wang, Z. G.; Niu, L. J.; Sheng, Y. B.; Xue, D. S. et al. Ti_3AlC_2, a candidate structural material for innovative nuclear energy system: The microstructure phase transformation and defect evolution induced by energetic heavy-ion irradiation. *Acta Mater.* **2020**, *189*, 188–203.
[32] Zhang, Y. F.; Peng, S. Y.; Wang, Y. H.; Guo, L. X.; Zhang, X. Y.; Huang, H. Q.; Su, S. H.; Wang, X. W.; Xue, J. M. Environment-dependent radiation tolerance of graphene transistors under proton irradiation. *J. Phys. Chem. Lett.* **2022**, *13*, 10722–10727.
[33] Guo, L. X.; Peng, S. Y.; Liu, Y.; Tian, S.; Zhou, W.; Wang, H.; Xue, J. M. Accurate measurement of defect generation rates in silicon carbide irradiated with energetic ions. *ACS Omega* **2023**, *8*, 41977–41982.
[34] Liu, Y. R.; Gao, Z. B.; Tan, Y.; Chen, F. Enhancement of out-of-plane charge transport in a vertically stacked two-dimensional heterostructure using point defects. *ACS Nano* **2018**, *12*, 10529–10536.
[35] Ahn, J.; Kyhm, J. H.; Kang, H. K.; Kwon, N.; Kim, H. K.; Park, S.; Hwang, D. K. 2D $MoTe_2/ReS_2$ van der Waals heterostructure for high-performance and linear polarization-sensitive photodetector. *ACS Photonics* **2021**, *8*, 2650–2658.
[36] Huang, H.; Wang, J. L.; Hu, W. D.; Liao, L.; Wang, P.; Wang, X. D.; Gong, F.; Chen, Y.; Wu, G. J.; Luo, W. J. et al. Highly sensitive visible to infrared $MoTe_2$ photodetectors enhanced by the photogating effect. *Nanotechnology* **2016**, *27*, 445201.
[37] He, R. J.; Wan, Y.; Zhao, P. J.; Guo, P.; Jiang, Z. Y.; Zheng, J. M. First-principles investigation of native point defects in two-dimensional Ti_3C_2. *Comput. Theor. Chem.* **2019**, *1150*, 26–39.
[38] Stoller, R. E.; Toloczko, M. B.; Was, G. S.; Certain, A. G.; Dwaraknath, S.; Garner, F. A. On the use of SRIM for computing radiation damage exposure. *Nucl. Instrum. Methods Phys. Res. Sect. B: Beam Interact. Mater. At.* **2013**, *310*, 75–80.
[39] Hu, C. Q.; Chen, H.; Li, L.; Huang, H.; Shen, G. Z. $Ti_3C_2T_x$ MXene-RAN van Der Waals heterostructure-based flexible transparent NIR photodetector array for 1024 pixel image sensing application. *Adv. Mater. Technol.* **2022**, *7*, 2101639.
[40] Ma, H. L.; Fang, H. J.; Liu, Y. Y.; Li, J. Q.; Jing, K.; Hong, J. W.; Wang, H. Fully transparent ultraviolet photodetector with ultrahigh responsivity enhanced by MXene-induced photogating effect. *Adv. Opt. Mater.* **2023**, *11*, 2300393.
[41] Di, Y. X.; Ba, K.; Chen, Y.; Wang, X. D.; Zhang, M. Q.; Huang, X. N.; Long, Y.; Liu, M. D.; Zhang, S. K.; Tang, W. Y. et al. Interface engineering to drive high-performance MXene/PbS quantum dot NIR photodiode. *Adv. Sci.* **2024**, *11*, 2307169.
[42] Ren, A. B.; Zou, J. H.; Lai, H. G.; Huang, Y. X.; Yuan, L. M.; Xu, H.; Shen, K.; Wang, H.; Wei, S. Y.; Wang, Y. F. et al. Direct laser-patterned MXene-perovskite image sensor arrays for visible-near infrared photodetection. *Mater. Horiz.* **2020**, *7*, 1901–1911.
[43] Montazeri, K.; Currie, M.; Verger, L.; Dianat, P.; Barsoum, M. W.; Nabet, B. Beyond gold: Spin-coated Ti_3C_2-based MXene photodetectors. *Adv. Mater.* **2019**, *31*, 1903271.
[44] Song, W. D.; Chen, J. X.; Li, Z. L.; Fang, X. S. Self-powered MXene/GaN van der Waals heterojunction ultraviolet photodiodes with superhigh efficiency and stable current outputs. *Adv. Mater.* **2021**, *33*, 2101059.
[45] Eginligil, M.; Cao, B. C.; Wang, Z. L.; Shen, X. N.; Cong, C. X.; Shang, J. Z.; Soci, C.; Yu, T. Dichroic spin-valley photocurrent in monolayer molybdenum disulphide. *Nat. Commun.* **2015**, *6*, 7636.
[46] Nie, C. B.; Yu, L. Y.; Wei, X. Z.; Shen, J.; Lu, W. Q.; Chen, W. M.; Feng, S. L.; Shi, H. F. Ultrafast growth of large-area monolayer MoS_2 film via gold foil assistant CVD for a highly sensitive photodetector. *Nanotechnology* **2017**, *28*, 275203.
[47] Wu, J. Y.; Chun, Y. T.; Li, S. P.; Zhang, T.; Wang, J. Z.; Shrestha, P. K.; Chu, D. P. Broadband MoS_2 field-effect phototransistors: Ultrasensitive visible-light photoresponse and negative infrared photoresponse. *Adv. Mater.* **2018**, *30*, 1705880.
[48] Choi, W.; Cho, M. Y.; Konar, A.; Lee, J. H.; Cha, G. B.; Hong, S. C.; Kim, S.; Kim, J.; Jena, D.; Joo, J. et al. High-detectivity multilayer MoS_2 phototransistors with spectral response from ultraviolet to infrared. *Adv. Mater.* **2012**, *24*, 5832–5836.
[49] Zhang, K.; Fang, X.; Wang, Y. L.; Wan, Y.; Song, Q. J.; Zhai, W. H.; Li, Y. P.; Ran, G. Z.; Ye, Y.; Dai, L. Ultrasensitive near-infrared photodetectors based on a graphene-$MoTe_2$-graphene vertical van Der Waals heterostructure. *ACS Appl. Mater. Interfaces* **2017**, *9*, 5392–5398.
[50] Azadi, S. K.; Zeynali, M.; Asgharizadeh, S.; Fooladloo, M. A. Investigation of the optical and electronic properties of functionalized Ti_3C_2 Mxene with Halid atoms using DFT calculation. *Mater. Today Commun.* **2023**, *35*, 106136.
[51] Lai, S.; Jeon, J.; Jang, S. K.; Xu, J.; Choi, Y. J.; Park, J. H.; Hwang, E.; Lee, S. Surface group modification and carrier transport properties of layered transition metal carbides (Ti_2CT_x, T: -OH, -F and -O). *Nanoscale* **2015**, *7*, 19390–19396.
[52] Urbančič, J.; Tomsič, E.; Chhikara, M.; Pastukhova, N.; Tkachuk, V.; Dixon, A.; Mavrič, A.; Hashemi, P.; Sabaghi, D.; Nia, A. S. et al. Time-of-flight photoconductivity investigation of high charge carrier mobility in $Ti_3C_2T_x$ MXenes thin-film. *Diam. Relat. Mater.* **2023**, *135*, 109879.
[53] Konstantatos, G.; Badioli, M.; Gaudreau, L.; Osmond, J.; Bernechea, M.; de Arquer, F. P. G.; Gatti, F.; Koppens, F. H. L. Hybrid graphene-quantum dot phototransistors with ultrahigh gain. *Nat. Nanotechnol.* **2012**, *7*, 363–368.
[54] Norgett, M. J.; Robinson, M. T.; Torrens, I. M. A Proposed method of calculating displacement dose rates. *Nucl. Eng. Des.* **1975**, *33*, 50–54.
[55] Lucchese, M. M.; Stavale, F.; Ferreira, E. H. M.; Vilani, C.; Moutinho, M. V. O.; Capaz, R. B.; Achete, C. A.; Jorio, A. Quantifying ion-induced defects and Raman relaxation length in graphene. *Carbon* **2010**, *48*, 1592–1597.
[56] Zeng, J.; Nie, C. B.; Zhang, H. D.; Hu, P. P.; Maaz, K.; Xu, L. J.; Zhai, P. F.; Yang, X. R.; Zhang, S. X.; Liu, J. Optimized photoelectric performance of MoS_2/graphene heterostructure device induced by swift heavy ion irradiation. *Appl. Surf. Sci.* **2024**, *642*, 158629.
[57] Hao, Q. Q.; Chen, L.; Wang, W. L.; Li, G. Q. Modulate the work function of MXene in MXene/InGaN heterojunction for visible light photodetector. *Appl. Phys. Lett.* **2024**, *125*, 012106.
[58] Patra, S.; Kiran, N. U.; Mane, P.; Chakraborty, B.; Besra, L.; Chatterjee, S.; Chatterjee, S. Hydrophobic MXene with enhanced electrical conductivity. *Surf. Interfaces* **2023**, *39*, 102969.